Received: 10 July 2020 | Revised: 31 August 2020 | Accepted: 2 October 2020

IET Image Processing

DOI: 10.1049/ipr2.12119

The Institution of Engineering and Technology WILEY

ORIGINAL RESEARCH PAPER

Unsupervised automated retinal vessel segmentation based on Radon line detector and morphological reconstruction

Meysam Tavakoli[1,2] | **Alireza Mehdizadeh**[3] | **Reza Pourreza Shahri**[4] | **Jamshid Dehmeshki**[5]

[1] Department of Physics, Indiana University-Purdue University, Indianapolis, IN, USA

[2] Radiation Oncology Department, University of Texas Southwestern Medical Center, Dallas, TX, USA

[3] Department of Biomedical Physics and Engineering, Shiraz University of Medical Sciences, Shiraz, Iran

[4] Department of Electrical Engineering, University of Texas at Dallas, Dallas, TX, USA

[5] Quantitative Medical Imaging Centre (QMIC), Faculty of Science, Engineering and Computing, Kingston University, London, UK

Correspondence
Meysam Tavakoli, Department of Physics, Indiana University-Purdue University, Indianapolis, IN, USA.
Email: corresponding.mtavakol@iu.edu

Abstract

Retinal blood vessel segmentation and analysis is critical for the computer-aided diagnosis of different diseases such as diabetic retinopathy. This study presents an automated unsupervised method for segmenting the retinal vasculature based on hybrid methods. The algorithm initially applies a preprocessing step using morphological operators to enhance the vessel tree structure against a non-uniform image background. The main processing applies the Radon transform to overlapping windows, followed by vessel validation, vessel refinement and vessel reconstruction to achieve the final segmentation. The method was tested on three publicly available datasets and a local database comprising a total of 188 images. Segmentation performance was evaluated using three measures: accuracy, receiver operating characteristic (ROC) analysis, and the structural similarity index. ROC analysis resulted in area under curve values of 97.39%, 97.01%, and 97.12%, for the DRIVE, STARE, and CHASE-DB1, respectively. Also, the results of accuracy were 0.9688, 0.9646, and 0.9475 for the same datasets. Finally, the average values of structural similarity index were computed for all four datasets, with average values of 0.9650 (DRIVE), 0.9641 (STARE), and 0.9625 (CHASE-DB1). These results compare with the best published results to date, exceeding their performance for several of the datasets; similar performance is found using accuracy.

1 | INTRODUCTION

The eye provides a keyhole view of the retinal vascular network. Many systemic diseases change the vascular network and could be diagnosed through this transparent window. Therefore, retinal vessel evaluation is increasingly used to establish retinal normality, and to diagnose/monitor diseases that exhibit retinal abnormality. Changes to the retinal vasculature are associated with conditions that include microaneurysms (MAs), hemorrhage (HEs) [1], and increasing levels of vessel tortuosity [2], that is a marker for diseases like diabetic retinopathy (DR) [3]. DR, as a common complication of diabetes, is the leading cause of blindness in the working population of Western countries and requires monitoring [4]. It is a silent disease and may only be recognized in a patient when retinopathy has progressed. Therefore, early screening of retinopathy can significantly reduce the incidence of blindness. In order to find DR symptoms, detection systems require the analysis of changes to the retinal vasculature. Indeed, the retinal vessel segmentation is the first step for the detection and diagnosis of the related DR lesions. In better words, early detection of DR can be screened by the analysis of retinal vessels [5]. Masking of the retinal vessels ensures that the vessels do not decrease the accuracy of systems in detection of the red lesions that are caused by DR [6]. Therefore, for such screening and detection systems, a fast and accurate segmentation algorithm for blood vessel detection is necessary. Evaluation and abnormality detection of the retinal vascular network undertaken by ophthalmologists is a time-consuming process, and associated with error and fatigue.

Moreover, clinical analysis based on an ophthalmologist's review may not be exactly repeatable. One possible solution for these problems is to use computer-assisted diagnosis systems [7–9] which apply automated computerized techniques to segmentation, leading to a more rapid and expedient detection [10, 11] and subsequent diagnosis. For this purpose, image processing techniques are required to extract suitable information

about changes to the vascular tree. In general, vessel segmentation is a critical step in screening for DR [12]. It is a cornerstone in the detection of other retinal landmarks, such as the optic nerve head (ONH) [13, 14] and the fovea [15]. Moreover, it is an important step in reducing the number of FPs (FPs) in the detection of MAs and HEs for the purpose of image registration [6] and the extraction of vasculature reference points.

This paper describes the evaluation of a fully automatic unsupervised algorithm for segmenting the retinal vascular tree using an approach based on the Radon transform (RT) originally developed in [16]. The contribution is fourfold: i) to improve the segmentation performance by suppressing FP detections, and false detections associated with MAs; ii) to validate the method on a much larger color dataset; iii) to investigate the applicability of an alternative quality measure, the structural similarity index (SSIM) [17]; iv) to evaluate performance on a large set of abnormal samples. The method is evaluated on three widely used retinal image datasets (DRIVE, STARE, CHASE-DB1) to enable performance comparisons with those of other researchers. In addition, we apply the method to a locally acquired dataset (MUMS-DB) that has a large proportion of DR cases, in order to evaluate the performance with a larger number of abnormal images. An important feature of the study is the use of the RT [18] to detect the vascular tree in retinal images, combine with the multi-overlapping windows, and morphological reconstruction. Compared with other line detectors, RT is less sensitive to noise in the image, because of the concept of integral operator that it has cancelled the intensity fluctuations due to noise [19]. As shown in the result section, our unique approach to detect blood vessels achieves higher performance than the reported unsupervised methods. Moreover, to evaluate the results of our segmentation in comparison with the other methods besides using receiver operating characteristic (ROC) curve, we used the concept of SSIM [17]. The results demonstrate a level of performance that matches or exceeds the best of current methods reported in the literature, using the conventional measure of accuracy, ROC curve, and area under the curve (AUC) analysis, and also reveal the benefits of a structural analysis of the vascular tree using SSIM.

The rest of the paper is organized as follows. The next section reviews other published studies in vessel segmentation. Section 3 introduces the material used in this study and explains the proposed method for retinal vessel segmentation. Section 4 provides an assessment of segmentation quality using the SSIM index. Section 5 presents the results and compares them to existing methods. The final section presents a discussion and conclusions.

2 | PREVIOUS WORKS

There is a substantial effort reported in the literature for the segmentation of blood vessels in fundus images [20–42]. A comprehensive review on existing methods in retinal vessel segmentation and available public datasets are presented in [43, 44]. In general, vessel segmentation algorithms can be classified into two broad categories: unsupervised and supervised methods [45]. A comparative survey of these two classes has been presented in [46]. Unsupervised methods can be further classified into techniques based on matched filtering [47, 48], morphological processing [9, 49], vessel tracking, multi-scale analysis [50, 51], line detectors [52], and model-based algorithms [53, 54]. Supervised segmentation methods are based on pixel classification such as the k-nearest neighbours (kNN) [55], Gaussian mixture models [56], support vector machines (SVM) [57], neural networks (NNs) [57], decision trees [27], and AdaBoost [58, 59]. They utilize ground truth data for the classification of vessels, based on given features.

The principle of matched filter detection in unsupervised methods was proposed in [47]. With this technique, the authors used a 2-D Gaussian-shaped template to search for vessel segments in all possible directions. The resulting image is thresholded to produce a binary representation of the retinal vasculature. Chakraborti et al. [48] applied an unsupervised segmentation approach that combined a 'vesselness' filter and matched filter using an orientation histogram. Vermeer et al. [53] achieved vessel detection by thresholding, after convolving the image with a 2-D Laplacian kernel. A general framework of adaptive local thresholding based on the use of a multi-threshold scheme, combined with a classification procedure to verify each resulting binary object, was applied by Jiang and Mojon [60].

An improved method for blood vessel segmentation using morphological component analysis was introduced by [42, 49]. Martinez-Perez et al. [50] presented an automated technique for retinal images based on a multi-scale feature extraction. The local maxima of the gradient magnitude and the maximum principal curvature of the Hessian tensor were used in a multi-pass region growing procedure. Zhang et al. [51] employed innovative rotating multi-scale second-order Gaussian derivative filters which are referred to as orientation scores for the enhancement and segmentation of blood vessels. Roychowdhury et al. proposed an iterative unsupervised retinal vessel segmentation algorithm that used an adaptive threshold and a region growing method with a stopping criterion to terminate the iteration [61].

Nguyen et al. proposed a vessel detection method based on line detection [52]. This approach was based on this fact that changing the length of a line detector makes line detectors with variety of scales. The final vessel segmentation results were achieved by combining line responses at varying scales. The combination of shifted filter responses (COSFIRE) for detection of bar-shaped structures in retinal images was presented by Azzopardi et al. [62]. Their approach was rotation invariant, where the orientation selectivity was determined from given vessel-like structures which suffered from difficult crossing cases. Lam and Yan [54] used the Laplacian operator to extract blood vessels and detect centerlines from the normalized gradient vector field, pruning noisy objects. Vessel continuity employs measures of width and orientation, iteratively computed in a local region near the current point, in order to track along the length of a vessel [63, 64].

Supervised approaches [28, 55, 57, 65] use a pixel classification method, referred to as a primitive-based method by Staal et al. [66]. This algorithm is based on the extraction of ridges,

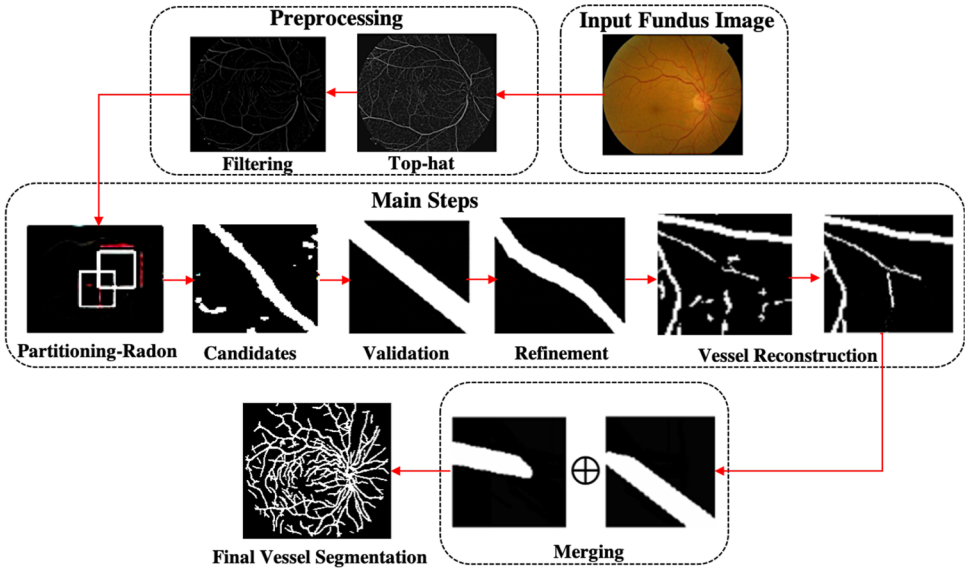

FIGURE 1 Block diagram of proposed method. Here we pictorially show the steps of our study. The details of each step is explained in the text

used as primitives for describing linear segments, named line elements. Sinthanayothin et al. [67] identified retinal vessels using a NN whose inputs were derived from principal component analysis of the image and edge detection of the first principal component. The kNN classifier was implemented by Niemeijer et al. [55]. In their method, from the green channel of the original image, a 31-component pixel feature vector was constructed with the Gaussian and its derivatives up to order 2 at 5 different scales, augmented with the grey level. Soares et al. [56] applied a Gaussian mixture model Bayesian classifier. By using the Gabor wavelet transform, multi-scale analysis was performed on the image. Ricci and Perfetti [57] utilized an SVM for classifying pixels as vessel or non-vessel. They applied two orthogonal line detectors along with the grey level of the target pixel to construct the feature vector. One of the best supervised methods was implemented by Fraz et al. [28] which was an ensemble classification system of boosted and bagged decision trees. The drawback of supervised classification is its need for a sufficient number of manually annotated training samples and it is not easy to generalize the trained models to meet the requirements of different datasets. More recent studies have successfully applied the concept of deep learning to the segmentation of the retinal vasculature [68–77].

The available literature broadly falls under hand-crafted methods and NN-based algorithm. As we explain in the result section, while NN-based approaches deliver good results in terms of accuracy and outperform humans occasionally, they need heavily parallelized hardware, e.g. GPU to run which is not available to all users. Hand-crafted methods, on the other hand, require a lot of domain expertise but are much computationally cheaper. Our method as a hand-crafted one improves the accuracy of the existing methods with high robustness without a lot of computations. This study describes an unsupervised vessel segmentation method for retinal images based on a combination of the RT, multi-overlapping windows, and a morphological reconstruction that extends our previous method [16]. The extension of our previous method is, first, evaluation of the algorithm with real color retinal databases. Here, we used images from four different databases (one rural and three public databases) instead of the previous one which was fluorescein angiography retinal images. Second, in the method section, we added morphological reconstruction to minimize FP pixels associated with other retinal lesions and landmarks. Finally, a means of measuring image quality called SSIM index, based on the human perception, was performed to more correctly determine image distortion than the commonly used method of mean squared error to benchmark the results of final segmentation. Results of the method are compared with normal images and those affected by DR. The goal of this work is to develop a complementary automated algorithm for detecting the retinal vessel network to support the detection of DR.

3 | PROPOSED METHODOLOGY

A pictorial flowchart of the proposed method is shown in Figure 1 and the individual processing steps are detailed in the following sub-sections.

3.1 | Materials

To evaluate the retinal vessel segmentation method described in this study, four datasets (one local and three publicly available) were used (see Table 1).

1) The first set (rural database) is named **MUMS-DB** (Mashhad University Medical Science Database). The MUMS-DB provided 120 retinal images including 100 cases with DR and 20 without DR or any systemic disease or ocular microvascular involvement. The images were obtained via a TOPCON (TRC-50EX) retinal camera at 50 degree field of view (FOV) and mostly obtained from the posterior pole view

TABLE 1 Details for the four datasets in this study

Database	Image size	FOV	Normal	Abnormal	No. of images
MUMS-DB	2896 × 1944	50	20	100	120
DRIVE	768 × 584	45	31	7	40
STARE	700 × 605	35	10	10	20
CHASE_DB1	999 × 960	30	–	28	28

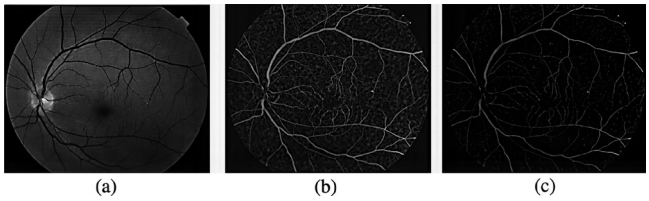

FIGURE 2 Preprocessing steps. (a) Fundus image from MUMS-DB. (b) Top-hat result. (c) Result of subtraction of top-hat and filtered top-hat image

(including ONH and macula) with a resolution of 2896 × 1944 pixels [78].

2) The second is the **DRIVE** database consisting of 40 images with a resolution of 768 × 584 pixels; 33 images have no signs of DR and 7 images showed signs of early or mild DR with a 45 degree FOV. For algorithms that operate in a supervised manner, this database is often divided into a testing and training set, each containing 20 images. For the test set, two specialists provided manual segmentations for each image [55].

3) The **STARE** database consists of 20 retinal images that were used initially by Hoover and Goldbaum. These images were captured at 35-degree FOV with an image resolution of 700 × 605 pixels. This database contains 10 images of normal retina and 10 images of diseased retina. [47].

4) The **CHASE-DB1** dataset [43] includes 28 fundus images with a resolution of 999 × 960 pixels, acquired from both the left and right eye. An ophthalmologist and human experts were asked to mark the vessels in all these images and these hand-labelled vessels were used as the ground truth (or gold standard) for this dataset.

3.2 | Preprocessing and image enhancement

A preprocessing (enhancement) step is used to increase the contrast between the vessel and the non-uniform background. The green channel of the RGB image is chosen as the input image (I), as it provides the greatest contrast between vessel and background. Intensity variations in the background of the fundus images can lead to poor vessel detection. For example, some background image regions can appear brighter than the foreground vessels. To deal with this problem, the image I is complemented by subtracting each intensity from the maximum (white) value. To create a more uniform background, a top-hat transform is then applied to the complemented image. The transformation uses a disk-shaped structural element whose diameter was empirically found to provide the best separation of vessel from background (d=10 pixels). Because the disk diameter depends on the input image resolution, various diameters were tested for the different datasets to evaluate the effect of that on final segmentation (see Section 5.2.1 for more details). The result of this first step of preprocessing is shown in Figure 2(b). Following application of the top-hat transform, an averaging filter (filter size=25 × 25 pixels) was used to suppress remaining intensity variations and point noise, which further helped in reducing FP detections. The results of the averaging are then subtracted from the top-hat transformed image. The final result of preprocessing is shown in Figure 2(c).

3.3 | Detection of retinal vessel

Blood vessels can be described as dark curvilinear objects against a lighter background, with indistinct edges. The retinal blood vessels are non-uniform in intensity, length, and width throughout the image. As a result, global detection methods are prone to failure. The algorithm described here applies analysis localized to sub-regions of the image where features exhibit more homogeneity. The algorithm is composed of five steps: image partitioning, local RT, vessel validation, vessel refinement, and vessel reconstruction. Further details involving steps 1–3 can be found in [16]. The retinal image is initially partitioned into small overlapping windows within which short sections of vessel will be detected and segmented. The RT is used to detect these short sections of vessel as line-like features, and to create a coarse estimate of the vessel orientation and width. Vessel sections detected in each window are accumulated over the entire image. Those parts associated with FP detections and microaneurysms, are suppressed used a vessel reconstruction method to create the final segmentation of the vascular tree. The algorithm is described in detail in the following sections.

3.3.1 | Image partitioning

The fundus image is partitioned into sub-image windows to ensure reliable detection of short sections of a vessel. The background and vessel pixels will exhibit the greatest homogeneity for a small window, but the window must be large enough to wholly contain the widest vessel sections, which is necessary for detection of the vessel section using the RT. Hence, the window size of ($n \times n$) is chosen to be at least twice the width of the thickest vessel in the image, which leads to a value for n that is approximately 2% of the full image width. In fact, the image size is our geometric feature that applies here. The hyperparameter that is most sensitive to image size is the window size (n). Here, image size is taking into account the image resolution and consequently window size differs with changing in image resolution.

One issue with windowing is that the vessel boundary might fall on the window edge. The windows are overlapped to ensure that the vessel will be more centrally located in the window

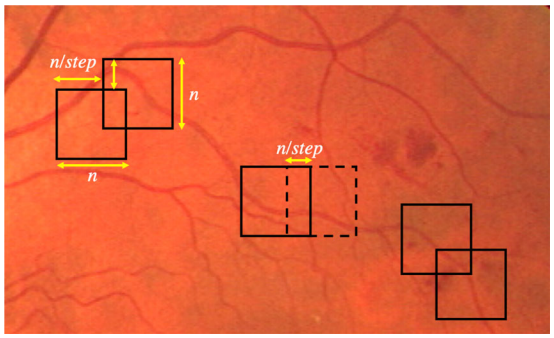

FIGURE 3 Overlapping windows. A window size and overlapping ratio (*n*, step)

in subsequent instances of the sliding window position. The degree of overlap is controlled by the value of the step size (step) of the sliding window. As shown in Figure 3, the step size can be expressed as a proportion of the window size. Overlapping windows ensure that each pixel is examined multiple times (actually, 'step' number of times in both the horizontal and vertical sliding direction) resulting in each pixel being processed up to n^2 times for a step size of 1. An experiment to assess the value of overlapped windows is described in Section 5.2.2.

3.3.2 | Local Radon transform

The RT is an algorithm that can used to locate line segments in an image, by projecting and integrating the image intensities through 180 degrees. Combination of local RT with overlapping windows is used here to detect and locate sections of vessel in the windows, where the contrast between the vessel and background is associated with peaks in Radon space: the longer the line in the image domain, the stronger the peak in the transform domain. The motivation behind using the RT is that it makes the algorithm less sensitive to noise than other methods, because variations in intensity due to noise tend to be removed by the process of integration. In the RT, each line gives a peak or a valley in Radon space. For the detected line, other features such as line width and line orientation can be directly extracted from the Radon matrix.

The RT of a function $f(x, y)$ which represents the greyscale density and the transformed function $f_\theta(s)$ is defined in Equation (1) [18].

$$f_\theta(s) = \int_0^y \int_0^x f(x,y)\delta(s - x\cos\theta - y\sin\theta)dxdy \quad (1)$$

Both x and y in Equation (1) are equal to the window size, n. However, a problem arises because there are more diagonal pixels than other directions. Therefore, the peak in the RT is more likely to appear in this diagonal direction. Hence, a circular mask is applied to the preprocessed sub-image, as shown in Figure 4. The vessel profile in which peak has occurred is considered a candidate that might contain a vessel. This profile is further analyzed for validation of a candidate vessel.

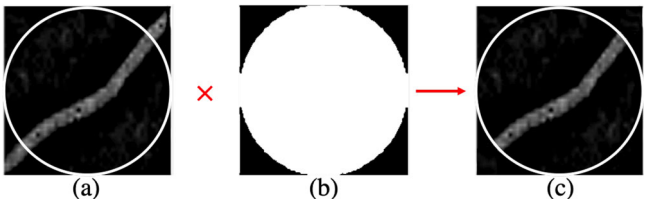

FIGURE 4 Masking process. (a) Preprocessed sub-image; (b) applied mask; (c) masked sub-image

TABLE 2 Comparison of segmentation performance with and without overlapping windows, measured across the four datasets

- Database	Without Overlap TPF	Without Overlap FPF	With Overlap TPF	With Overlap FPF	No. of images
MUMS-DB	0.5023	0.2510	0.9562	0.2020	120
DRIVE	0.6715	0.2510	0.9613	0.2020	20
STARE	0.6073	0.2510	0.9589	0.2020	20
CHASE-DB1	0.5913	0.2510	0.9512	0.2020	28

3.3.3 | Vessel validation

In this section, the peak amplitude in Radon space is compared with a predefined threshold (Th) (see Table 2). If the peak amplitude is larger than the threshold, the detected vessel is confirmed, otherwise the next projection is analyzed. This process is repeated for θ between 0 and π in increments of 6 degrees. At this point, or if a vessel section is successfully detected, the window is advanced by 'step' pixels and the RT detection process is repeated.

When a vessel is successfully found, the algorithm calculates the vessel's width (w), $w = i_{\max} - i_{\min} + 1$, and its orientation (with respect to the window) as well as the intersection of its start and end points with the window border. A binary detection mask is constructed using these parameters to create an initial (coarse) segmentation of the vessel section, referred to as the local vessel map.

Figure 5 plots a section of the RT projection profile that passes through the detected peak in RT space. The peak's index,

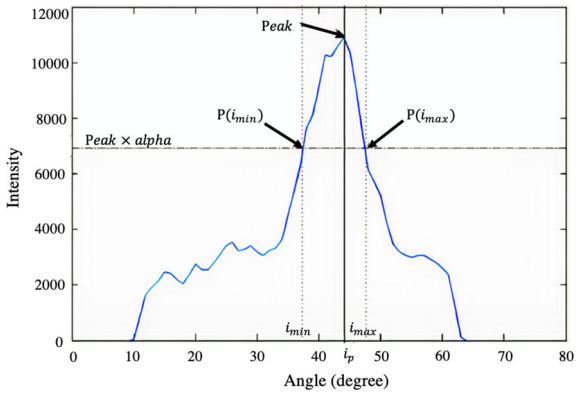

FIGURE 5 Sample Radon profile. Projection profile of Radon transform (P) for a peak located at $\theta = 45$ degrees (for image window shown in Figure 4(c)

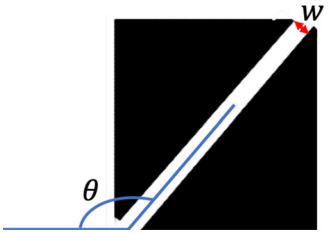

FIGURE 6 Local vessel mask calculated from profile in Figure 5

i_p, determines the orientation of the sub-vessel's centerline and the interval $[i_{\min}, i_{\max}]$, is used to approximate the sub-vessel's width ($w = i_{\max} - i_{\min} + 1$). The values of $[i_{\min}, i_{\max}]$ are estimated as a proportion of the peak height as follows:

$$P(i_{\min}) = P(i_{\max}) = \alpha \times P(i_p) \tag{2}$$

where α is a constant ($0 < \alpha < 1$) which is chosen empirically (see Table 2). The sub-vessel mask is created using the projection angle (θ) width determined $i_{\max}$ and $i_{\min}$. Figure 6 depicts the local vessel mask (LVM) created for the vessel segment shown in Figure 4 based on the peak detected in Figure 5. In the next section, this mask will be used to define the mean intensities of vessel and background.

3.3.4 | Vessel refinement

The LVM provides a coarse segmentation of the vessel segment, but a more accurate refinement is generated by intensity thresholding. The mask is used to define two image regions: background and vessel. The mean pixel intensity is computed for these two regions and the intensity threshold (T_{BSI}; Table 2) that best separates them is defined by

$$T_{\text{BSI}} = \begin{cases} 1, \text{ if } & T > \frac{m_1 + m_2}{2} \\ 0, \text{ else} \end{cases} \tag{3}$$

Here, the first mean (m_1) is the mean of those pixels in window which their associated pixels in LVM place on white ribbon. The second mean (m_2) is the mean of those pixels in window which their corresponding pixels in LVM set on the black background. The result of thresholding the pixel intensities creates the binary sub-image (BSI). Because thresholding is a noise-sensitive process. the LVM is used to suppress detections outside the vessel region defined by the white pixels of the LVM. The result is named the fine local mask (FLM) and is generated by a logical ANDing of the LVM and BSI images. Figure 7(d) and (h) shows the final vessel segmentation result for the image window shown in Figure 4.

$$FLM(i,j) = LVM(i,j) \textbf{ AND } BSI(i,j) \quad [i,j = 1,2,\dots,n] \tag{4}$$

Finally, the FLMs associated with all the image windows are merged to obtain a complete vessel segmentation of the input image. Figure 8 depicts the merging of two overlapping FLM's, highlighting the capability of the algorithm to cope with the failure of the individual segmentation to reliably detect the vessel region in each window. The merging is implemented as a logical OR of the FLM windows.

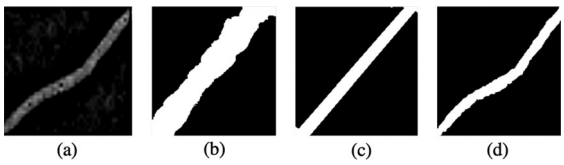

FIGURE 7 Vessel refinement steps. An example of window analysis: (a) preprocessed sub-images; (b) binary sub-images (BSI); (c) local vessel masks (LVM); (d) fine local masks (FLM) of sub-images

FIGURE 8 Merging sub-images. Logical OR of sub-images of vessel refinement

3.3.5 | Vessel reconstruction

Vessel reconstruction analyzes the merged FLM images to minimise FP pixels-associated HEs, exudates (EXs), or MAs that are detected with the vessel tree whilst extending the connectivity of the vessel tree. Figure 9(b) and (f) shows examples of an FLM image with disconnected vessel fragments and FP detections. An iterative conditional dilation is used to apply a connectivity test to identify those elements that belong to the vessel tree, and unconnected false detections that can then be eliminated [Figure 9(c) and (e)].

The conditional dilation uses two binary images: a marker image that is used as a seed for the reconstruction process [9, 79]; and a mask image that constrains the dilation process to only add pixels that are part of the vessel tree. The mask image is the FLM created using the steps described in the previous section. The marker image is created using the same steps as the FLM, but a more stringent threshold is used for vessels detected by the RT. Hence, the mask image will contain only the more prominent and thicker vessels that are guaranteed to form part

FIGURE 9 Vessel reconstruction steps. (a) Original sub-images; (b) mask sub-images; (c) marker sub-images; (d) final result of vessel segmentation for the sub-images

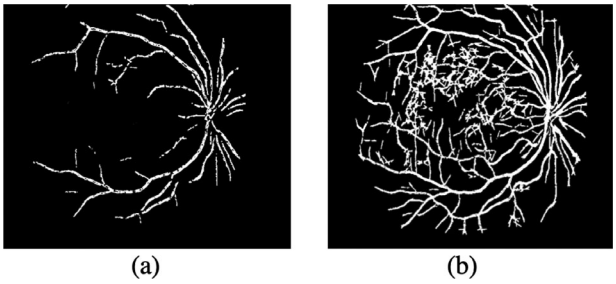

FIGURE 10 Mask and marker sample images. Conditional dilation masks: (a) marker image; (b) mask image or FLM image

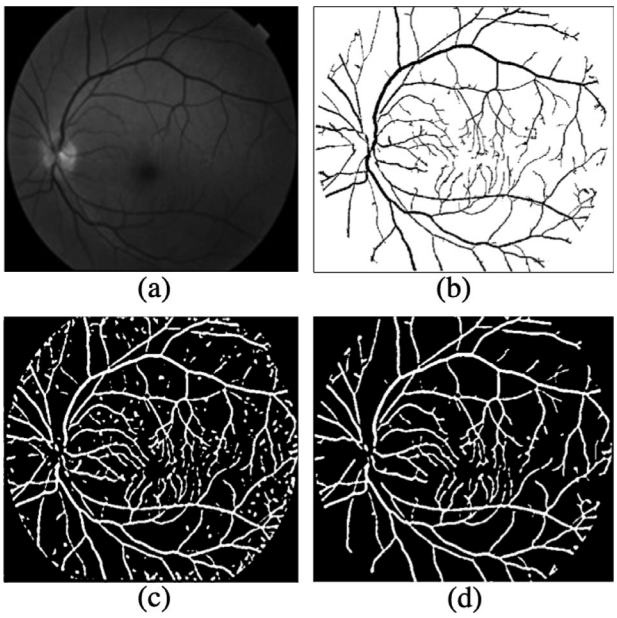

FIGURE 11 Final vessel segmentation. An example of vessel reconstruction for entire image: (a) original image from the MUMS-DB dataset; (b) manual vessel segmentation (ground truth); (c) vessel segmentation results with false positives, before applying morphological reconstruction; (d) accurate segmentation result after applying reconstruction

of the vessel tree. By using the marker image as the seed for the conditional dilation, and the FLM image to ensure the dilation operator cannot grow beyond the FLM mask, the FP regions can be found and eliminated. Figure 10 shows an example of the two image masks used for conditional dilation; the threshold value used for the marker image is $T_{\text{marker}} = 1.5$ Th; its value is empirically determined (see Table 2).

Figure 11 shows the results of vessel reconstruction on two examples. Since MAs or any FPs are separated from vessels and do not exist in the marker image, they do not appear in the final vessel map that is the output of conditional dilation and hence this morphological reconstruction removes all unconnected components associated with FPs from the final binary image.

The extracted blood vessels were checked by an independent ophthalmologist and the algorithm was evaluated subjectively.

4 | VESSEL SEGMENTATION ASSESSMENT USING STRUCTURAL SIMILARITY INDEX

The AUC and accuracy are widely used to assess the effectiveness of segmentation algorithms, providing single measures of performance that can easily be compared. Based on the hypothesis that the human visual system is well adapted to extracting structural information from the viewing field, an image quality measure is performed for retinal segmentation, based on the structural similarity (SSIM) measure [17, 80]. This measure of structural information change can provide a good approximation to understand image distortion as compared to conventional methods such as mean squared error that can be weakly correlated with human visual perception; also, its values for the same images do not inherently contain the same error. For the SSIM method, an objective image assessment can be classified according to the availability of an original image (the manual segmentation in our case) with which the automated segmentation image is to be compared. The motivation behind the SSIM approach for measuring retinal vessel segmentation quality is that ROC curves are not perfectly designed for detection of imperfections or noise and errors in the segmented images. Instead, the SSIM extracts information to exploit the structure (segmented vessels) of the original images. Based on this observation, it makes sense that a useful perceptual quality metric would emphasize the structure of scenes. In the SSIM approach, the structural part is sensitive to distortions or any changes that overwhelm natural spatial correlation of an image, such as artefacts and noise [81]. In general, the SSIM distinguishes between structural and nonstructural changes or distortions, giving results that agree with perception visibly distorted images. It takes values in the range 0.0 to 1.0, where zero corresponds to a loss of all structural similarity info and one means having an identical copy of the original image [80]. Just as an example for our study, Figure 16 shows a sample of the quality assessment of retinal vessel segmentation using SSIM index. The reason for greater success in quality assessment lies in the fact that the SSIM approach separates the task of similarity measurement into three categories: luminance, contrast, and structure. The first two, luminance and contrast, are constant in our case because our final segmented image is a binary image. The structure category (which is related to our segmented vessels) is particularly sensitive to noise (i.e. MAs and FPs) in the final segmentation results and this has a more significant effect on the SSIM measure than the ROC analysis [82]. As defined in [17], the structural information in an image is independent of the average luminance and contrast. Since luminance and contrast do not change in the segmentation results, the local luminance and contrast is used for our definition. The SSIM value is given by

$$\text{SSIM}(x,y) = \left[\frac{2\mu_x\mu_y + C_1}{\mu_x^2 + \mu_y^2 + C_1}\right]^{\alpha} \cdot \left[\frac{2\sigma_x\sigma_y + C_2}{\sigma_x^2 + \sigma_y^2 + C_2}\right]^{\beta} \cdot \left[\frac{\sigma_{xy} + C_3}{\sigma_x\sigma_y + C_3}\right]^{\gamma} \quad (5)$$

where $\alpha > 0, \beta > 0$, and $\gamma > 0$ are parameters used to weight the importance of each component. In this paper, α, β, and γ are given equal weighting and are all set to a value of 1.

The standard deviation $\sigma_{xy} = \frac{1}{N-1}\sum_{i=1}^{N}(x_i - \bar{x})(y_i - \bar{y})$ and C_1, C_2, C_3 are three constants related to the dynamic range of the pixel values. An important point is that the three components are relatively independent. Because the segmentation is local (local RT), the quality assessment will be more useful rather than if we had applied a global SSIM index locally. This index compares automated segmented images with manual segmentations (as our gold standard). So the closer the index value is to 1, the greater the similarity between the ground truth and the segmented images.

5 | EXPERIMENTAL RESULTS

Two standard methods are used to assess the effectiveness of the proposed method and to enable comparison with results reported by others: ROC analysis and SSIM analysis. ROC curves illustrate the tradeoff between sensitivity (Se) and specificity (Sp) for a range of thresholds and enable the identification of an optimal value [83]. However, different classification goals might make the selection of one point on the curve more appropriate for one task whilst another point may be more suitable for a different task. Hence, assessment using the ROC curve is a way to evaluate the model independent of the choice of threshold.

The algorithm was evaluated in terms of the true positive fraction (TPF) given by (Se), and the false positive fraction (FPF), given by (1-Sp). Also, the accuracy was determined as a measurement providing the ratio of well-classified pixels. The results for the automated method compared to the ground truth or gold standard (GS) were calculated for each image. These metrics are defined as follows:

$$\begin{aligned} \text{Sensitivity (Se)} &= \frac{\text{TP}}{\text{TP} + \text{FN}} \\ \text{Specificity (Sp)} &= \frac{\text{TN}}{\text{TN} + \text{FP}} \\ \text{Accuracy (Acc)} &= \frac{\text{TP} + \text{TN}}{\text{TP} + \text{FN} + \text{TN} + \text{FP}} \end{aligned} \tag{6}$$

where TP is true positive, TN is true negative, FP is false positive and FN is false negative, the same as in [59, 84].

5.1 | Parameters tuning

In this study, several different retinal image datasets have been used to evaluate the performance of the proposed segmentation algorithm. Table 1 summarises details of the four datasets. For each dataset, we have some images for fine-tuning of algorithm parameters. The purpose of parameter tuning is to set all the parameters which our segmentation has maximum accuracy. After fixing the parameters of the algorithm by using appropriate set, the algorithm was tested in each image of our databases.

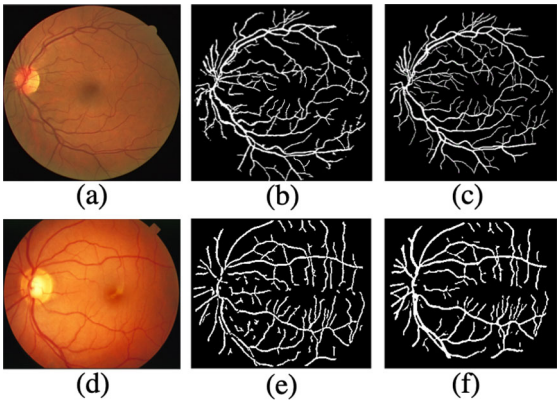

FIGURE 12 Final vessel segmentation for public datasets. (a) and (d) Input image from DRIVE and STARE; (b) and (e) automatic segmentation results; (c) and (f) manual segmentation image (ground truth)

The DRIVE dataset comprises 40 retinal images and includes 20 images that have a hand-labelled segmentation and a further 20 unlabelled images. The labelled set is used as the tuning set and the remaining 20 form the test set.

For the other three datasets (STARE, CHASE-DB1, and MUMS-DB), there is no distinction between images that are used separately for tuning or testing. In the published studies, there are two ways to determine tuning and test sets. The first one is called the random samples method which builds randomly the tuning and testing sets and is used in most of the studies [57, 85]. The problem with this approach is that there is overlap between these two sets that raises a concern of excessively optimistic results [68]. The second approach is called leave-one-out [56, 66] which we used in this study. With this technique, each image is tested by using a network model that is trained on the other images. Hence, for the STARE dataset, one image is tested using the model trained on the other 19 retinal images. The advantage of this method is that the tuning and testing images do not overlap and the networks require tuning for all images in the dataset. Figure 12 shows the results of vessel detection related to three sample images from the public datasets.

5.2 | Comparison of the results of TPF and FPF

One validation is related to the TPF and the FPF. The validation of our segmentation was based on hand-labelled images as the manual segmentation or GS. The TPF is defined as the ratio of TP to the total number of vessel pixels in GS. The FPF is calculated by dividing the number of FP by the total number of non-vessel pixels in GS. The characteristic of perfect segmentation is TPF = 1 and FPF = 0.

5.2.1 | Setting the preprocessing parameters

The important characteristics in colour retinal images are colour and contrast (especially for the blood vessels). Uneven

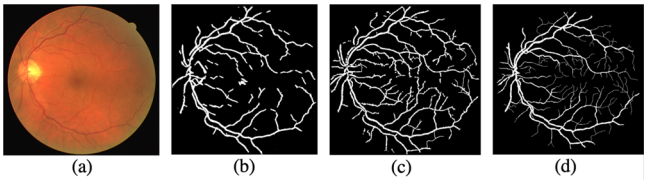

FIGURE 13 Evaluating effect of preprocessing. (a) Input image from DRIVE; (b) automatic segmentation results without preprocessing; (c) automatic segmentation results with preprocessing; and (d) manual segmentation image (ground truth)

TABLE 3 Comparison with and without vessel reconstruction in the four databases

- Database	Without TPF	Reconst. FPF	With TPF	Reconst. FPF	No. of images
MUMS-DB	0.9702	0.3544	0.9562	0.2020	120
DRIVE	0.9795	0.3544	0.9613	0.2020	20
STARE	0.9723	0.3544	0.9589	0.2020	20
CHASE_DB1	0.9673	0.3544	0.9512	0.2020	28

illumination causes noise in this images. To reduce the effect of noise in retinal image, we need to preprocess this image to enhance the quality. In such case, preprocessing the image can give better results in final segmentation or detection.

At the beginning, we need to check the effect of preprocessing. To evaluate the image quality of the preprocessed images after applying top-hat, we need to prove that preprocessing does not affect the vessel pixels. For this purpose, as you see in Figure 13, we compare the results of vessel segmentation with and without preprocessing first. Using the concept of *Se* and *Sp* related to ROC curves, the accuracy of vessel segmentation without preprocessing dropped by at least 15%.

After evaluating the effect of preprocessing, the next step is assessing the sensitivity of the parameters that control the preprocessing steps. With the top-hat algorithm, in order to avoid removal of portions of the vessels, it is necessary to apply a large structural element. However, a large structural element increases the background noise. A reasonable compromise sets the size of the structural element to be the maximum size of the primary vessels. The algorithm was evaluated using constant averaging filter size (25 pixels) and a range of structural elements of varying sizes. The segmentation result after vessel reconstruction was stable for sizes of 10–50 pixels (varied in increments of 10 pixels), but for values outside this range, the accuracy of vessel segmentation dropped by at least 10%. A second experiment varied the size of the averaging filter. For this, the structural element for the top-hat was fixed at 10 pixels and for filter sizes from 40 to 100 pixels (in increments of 10 pixels), the result (as shown in Table 3) remained stable, but below 40 pixels, segmentation performance dropped by 5%–10%. Hence, a value of 25 pixels was chosen as the most effective and efficient value for the remainder of the experiments for all databases.

TABLE 4 Parameters used for ROC analysis of optimum Th value

Database	No. of images	Window size (n)	Step	Th	α	T	T_{marker}
MUMS-DB	120	62	5	[0,5]	0.5	0.5	1.5Th
DRIVE	20	15	5	[0,5]	0.5	0.5	1.5Th
STARE	20	18	5	[0,5]	0.5	0.5	1.5Th
CHASE_DB1	28	30	5	[0,5]	0.5	0.5	1.5Th

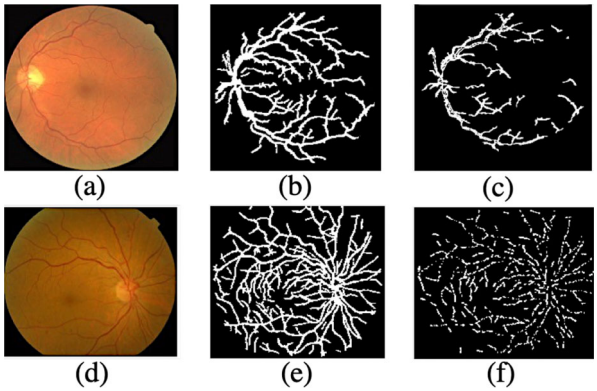

FIGURE 14 Effect of overlapping windows. (a) and (d) Input image from DRIVE and MUMS-DB; (b) and (e) results for a window step of 5 (80% overlap); (c) and (f) results with a window step of 1 (no overlap)

5.2.2 | Effectiveness of overlapping windows

This experiment assesses the value of the overlapping widows. As in Section 5.2.1, the evaluation considers the segmentation after vessel reconstruction. Table 4 shows the result of a step size of 1 (i.e. no overlap) compared with a step size of 5 (i.e. 80% overlap). As can be seen, segmentation accuracy drops below 70% without overlap, considerably poorer than the result when overlapping is employed. This lower performance is reflected in Figure 14(c) and (f) where the fragmented appearance of the final segmentation result is clearly visible. This experiment demonstrates the importance of using overlapping windows to achieve a robust segmentation result.

5.3 | Comparing the results of ROC curves in four databases

This experiment investigates the optimal value for the threshold value (Th) that is used to select valid peaks in the RT and determine the presence of a valid vessel segment within an image window. This optimal value is determined by using ROC curves [a plot of TPF (Se) versus FPF (1-Sp)] generated using varying values Th over the range [0:5], on vessel segmentation performance for each of the datasets. Figure 15 superimposes the results for all four datasets using the set of parameters shown in Table 2.

The ROC curve, which provides a graphical representation of classifier performance, can be reduced to a single value that

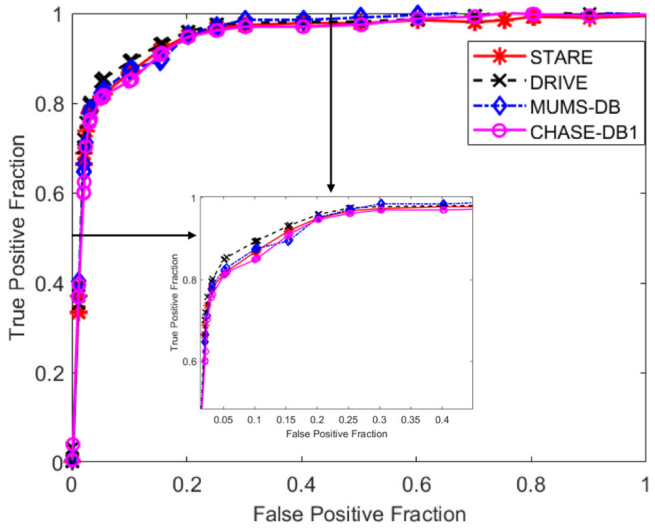

FIGURE 15 ROC curves for all databases. ROC curves for values of Th in the range [0:5] on the four datasets

describes an algorithm's performance [86] by calculating the AUC, which is 1 for a perfect system,. The AUC measured separately for images from the four datasets is 95.98% for MUMS-DB, 97.39% for DRIVE, 97.01% for the STARE, and 97.12% for CHASE DB1. Segmentation performance measured using accuracy [Equation (6)] is 0.9456, 0.9688, 0.9646, and 0.9475, respectively, for MUMS-DB, DRIVE, STARE, and CHASE-DB1.

Finally, the proposed method was compared with other studies reported in the literature, both supervised and unsupervised, that have used the three public datasets [28, 48, 49, 51, 56, 57, 59, 62, 87–91]. Table 5 compares the results for accuracy whilst Table 6 shows AUC values. From both the accuracy and AUC results, our method is demonstrated to be effective for vessel segmentation on these datasets. Its application to the STARE dataset resulted in the third highest AUC among other algorithms (behind Marin et al. [59] and Fraz et al. [28]) and the second best for the DRIVE dataset (only behind Fraz et al. [28]). For the CHASE-DB1, the results were the highest for both accuracy and AUC. It can be noted that these results (by comparison with other studies) are obtained using a large proportion of images with pathological signs; also, abnormalities and poorer image quality are more common in the STARE dataset [47]. Compared to all the unsupervised methods, our approach achieved better results, as shown in Tables 5 and 6. In the case of accuracy, our approach was the highest compared with all other methods on the STARE database (same as Ricci and Perfetti [57]) and highest among those performed on images from the DRIVE and CHASE-DB1 datasets.

5.4 | Evaluation of the approach with abnormal images

The accuracy of vessel segmentation algorithms can be strongly dependent on the presence of abnormalities such as red lesions (MAs and HEs) and bright lesions (exudates) in the retinal images [6, 56, 57]. Table 7 compares the results on two images from the STARE database that exhibit notable red and bright lesions, with results from the literature [55, 57, 61, 94]. Our method matches the performance of Roychowdhury et al. [61] and outperforms all other approaches except the perceptive transform-based method proposed by Lam et al. [94]. However, their method is more computationally expensive.

TABLE 5 Performance comparison results to other methods' accuracy

Type	Methods	DRIVE	STARE	CHASE_DB1
	Franklin and Rajan [21]	0.9503	–	–
	Niemeijer et al. [55]	0.9417	–	–
	Thangaraj et al. [65]	0.9606	0.9435	0.9468
	Staal et al. [66]	0.9441	0.9516	0.9467
Supervised	Soares et al. [56]	0.9466	0.9480	–
	Ricci and Perfetti [57]	0.9595	0.9646	–
	Marin et al. [59]	0.9452	0.9526	–
	Fraz et al. [28]	0.9480	0.9534	0.9469
	Chaudhuri et al. [12]	0.8773	–	–
	Odstrcilik et al. [20]	0.9340	0.9341	–
	Shahid and Taj [92]	0.9580	0.9513	–
	Panda et al. [30]	0.9539	0.9424	–
	Farokhian et al. [36]	0.9392	–	–
	Hoover et al. [47]	–	0.9275	–
	Jiang and Mojon [60]	0.8911	0.9009	–
	Cinsdikici and Aydin [93]	0.9293	–	–
	Mendonca et al. [9]	0.9463	0.9479	–
	Martinez-Peres et al. [50]	0.9344	0.9410	–
Unsupervised	YQ Zhao et al. [25]	0.9540	0.9560	–
	Biswal et al. [37]	0.9500	0.9500	–
	Khomri et al. [41]	0.9450	0.9400	–
	Zhang et al. [51]	0.9476	0.9554	–
	Roychowdhury et al. [61]	0.9494	0.9560	0.9467
	Azzopardi et al. [62]	0.9442	0.9497	0.9387
	Oliveira et al. [89]	0.9464	0.9532	–
	Imani et al. [49]	0.953	0.951	–
	Y Zhao et al. [87]	0.9523	0.9590	–
	Chakraborti et al. [48]	0.9370	0.9379	0.9304
	Javidi et al. [91]	0.9450	0.9517	–
	Neto et al. [34]	0.8787	0.8616	–
Proposed method	Our method	**0.9688**	**0.9646**	**0.9475**

5.5 | Evaluation using SSIM index

The SSIM index was computed for all four datasets, with average values for each dataset of 0.9460, 0.9650, 0.9641, and

TABLE 6 Performance comparison results to other methods' AUC

Type	Methods	DRIVE	STARE	CHASE_DB1
	Niemeijer et al. [55]	0.9294	–	–
	Thangaraj et al. [65]	0.8884	0.8938	0.7971
	Staal et al. [66]	0.9520	–	–
Supervised	Soares et al. [56]	0.9614	0.9671	–
	Ricci and Perfetti [57]	0.9633	0.9680	–
	Marin et al. [59]	0.9588	**0.9769**	–
	Fraz et al. [28]	**0.9747**	0.9768	0.9712
	Chaudhuri et al. [12]	0.7878	–	–
	Odstrciliket al. [20]	0.9519	0.9569	–
	Shahid and Taj [92]	0.850	0.870	–
	Farokhian et al. [36]	0.9530	–	–
	Hoover et al. [47]	–	0.7590	–
	Jiang et al. [60]	0.9327	0.9298	–
	Cinsdikici and Aydin [93]	0.9407	–	–
	YQ Zhao et al. [25]	0.8620	0.8740	–
Unsupervised	Zhang et al. [51]	0.9636	0.9614	–
	Roychowdhury et al. [61]	0.9672	0.9673	0.9623
	Azzopardi et al. [62]	0.9614	0.9563	0.9467
	Oliveira et al. [89]	0.9513	0.9544	–
	Zhao et al.[87]	0.8610	0.881	–
	Chakraborti et al. [48]	0.9419	–	–
Proposed method	Our method	**0.9739**	**0.9701**	**0.9712**

TABLE 7 Comparison of segmentation performance on two abnormal samples from the STARE dataset

Methods	[47]	[60]	[56]	[53]	[94]	[61]	Proposed method
ACC	0.9211	0.9352	0.9425	0.9278	0.9556	0.9535	**0.9536**
AUC	0.7590	0.9343	0.9571	0.9187	0.9707	0.9638	**0.9638**

0.9625 for MUMS-DB, DRIVE, STARE, and CHASE-DB1, respectively. Figure 16 shows the change in the SSIM index (for a single exemplar image) across a range of vessel detection (Th) thresholds, from Th=[0.6 1.5] as follows: Th=0.6, SSIM= 0.9621; Th=0.8, SSIM= 0.9423; Th=0.9, SSIM= 0.9407; Th=1, SSIM= 0.9378; Th=1.5, SSIM= 0.7856. The index peaks with a value of 0.9621 at a Th=0.6.

Table 8 presents the averaged SSIM value for 10 images randomly selected from the four datasets, in order to illustrate the narrow variance of the measure across the datasets.

Finally, to compare some other methods with our method in terms of SSIM index, we evaluated the SSIM values for these studies and our proposed method. Table 9 presents this result for five random images from public datasets.

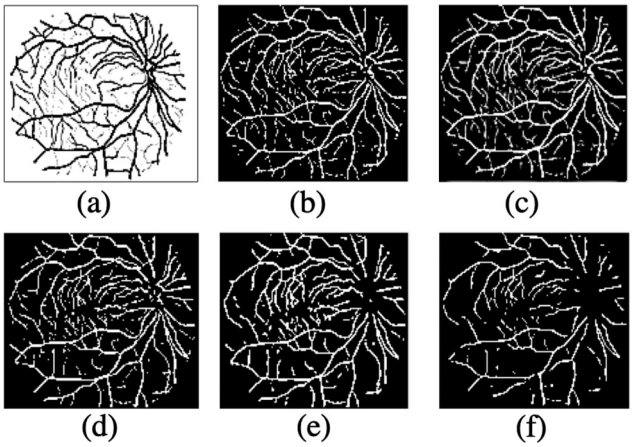

FIGURE 16 SSIM values. Variation of t and effect of that in vessel detection. (a) Input image; (b) Th=0.6, SSIM= 0.9413; (c) Th=0.8, SSIM=0.9621; (d) Th=0.9, SSIM= 0.9407; (e) Th=1, SSIM= 0.9378; (f) Th=1.5, SSIM= 0.7856

6 | DISCUSSION

This study has presented and validated an algorithm to segment the retinal blood vessel network in a fully automatic fashion. It combines multi-overlapping windows, with the RT by adding morphological reconstruction, and improved vessel refinement applied to colour retinal imagery that extends our previous work [16], beyond just fluorescein angiography retinal images, and removes with greater clarity the FP vessel detection. In addition, the extension of our previous method is a significant improvement in accuracy from our antecedent paper and is commensurate to previous research methods, listing a comparison accuracy table (Table 5). Further validity is gained by appreciably increasing the amount of data from our previous work, implementing images from four different databases (one rural and three public databases) instead of the previous one. Finally, a means of measuring image quality called SSIM, based on the human perception, is performed to more correctly determine image distortion than the commonly used method of mean squared error.

Previous approaches for retinal vessel segmentation can be classified into supervised- and unsupervised-based methods. The proposed study is an approach within the latter class. According to the results of TPF, FPF, and ROC curve analysis, the method is shown to outperform many of the alternative methods reported in the literature over the past 10 years. Tables 5 and 6 present an overall performance on previously published vessel segmentation approaches in terms of accuracy and and AUC, respectively, for DRIVE and STARE databases. From the measurement of AUC, as shown in Table 6, our method performs better than Staal et al. [66], Niemeijer et al. [55], Soares et al [56], and Ricci and Perfetti [57] in the supervised methods and Chaudhuri et al. [12], Jiang et al. [60], and Cinsdikici and Aydin [93] in the unsupervised methods. In the case of the STARE, our results are comparable with Marin et al. [59] and Fraz et al. [28]. In terms of accuracy, our approach performs better than Hoover et al. [47], Martinez-Prez et al. [50], and Chaudhuri et al. [12] on STARE images. In DRIVE database, it outperforms Jiang et al. [60], Cinsdikici and Aydin

TABLE 8 Evaluation using SSIM index for 10 sample images from the four datasets

Image	1	2	3	4	5	6	7	8	9	10	Average
MUMS-DB	0.9623	0.9713	0.9589	0.9656	0.9697	0.9778	0.9726	0.9689	0.9610	0.9534	**0.9662**
DRIVE	0.9684	0.9691	0.9602	0.9711	0.9666	0.9579	0.9693	0.9619	0.9592	0.9654	**0.9649**
STARE	0.9598	0.9661	0.9673	0.9622	0.9590	0.9631	0.9612	0.9703	0.9654	0.9627	**0.9637**
CHASE_DB1	0.9650	0.9652	0.9670	0.9589	0.9602	0.9614	0.9630	0.9591	0.9577	0.9631	**0.9621**

TABLE 9 Comparison our algorithm using SSIM index for five sample images from the public datasets with other methods

Methods	[47]	[59]	[56]	[62]	[94]	[61]	Proposed method
DRIVE	0.8816	0.9488	0.9593	0.9619	0.9640	0.9630	**0.9645**
STARE	0.7912	0.9433	0.9312	0.9103	0.9654	0.9627	**0.9639**
CHASE_DB1	0.8592	0.9514	0.9530	0.9525	0.9620	0.9331	**0.9620**

[93], Zana et al. [95], Gang et al. [96], and Martinez-Prez et al. [50]. Accurate vessel detection, based on a robust algorithm, in terms of vessel widths and continuity, allows detection of disease-affected morphological changes such as change in diameters, tortuosity, length, and angle of bifurcations [97] and even changes in topological structure. [98]. The obtained results show the high accuracy of our approach in vessel segmentation and its robustness against noise. As we have shown in Figure 12, our method extracted both thick and thin vessels appropriately even in low contrast regions.

In general, although most of supervised approaches have better results in vessel segmentation, they are dependent on the training data to learn the nets and also sensitive to false edges [61]. It was observed that, for instance, in Ricci and Perfetti [57], by dropping the training images, the performance of accuracy strongly decreased from 0.9595 to 0.9266 on DRIVE database and 0.9646 to 0.9452 on STARE database [59]. Moreover, they need heavily parallelized hardware, e.g. GPU to run which is not available to all users. Whilst most of the existing methods, such as [52, 54, 56], have good segmentation results on healthy retinal images, some have low accuracy with abnormal pathology. For this reason, the method presented in this paper is evaluated on a dataset, STARE, with significant pathology, yielding good segmentation results in both accuracy (Table 5) and AUC (Table 6). To test our approach using high-resolution images, a new database (MUMS-DB) was utilized that contained at least three times the number of images in the most widely used public datasets. Although the performance on this database was lower than the other three public datasets (on average about 4% less), it still segmented vessels with high accuracy and AUC (greater than 90%).

Furthermore, most of studies in vessel detection are based on morphological processing and vessel tracking, where many of them mandate detection of retinal land marks such as the ONH and make a key point of this in their algorithms. Nevertheless, one of the significances of our algorithm is that it is unnecessary to identify the location of the ONH for vessel segmentation. The reason for that is our vessel segmentation method works by this broad assumption that blood vessels could be treated as piece-wise linear structure and be detected by RT. Therefore, this eliminates the need for ONH detection. Another advantage of our algorithm, unlike some approaches, such as [51, 53, 61] which consider small MAs close to the vasculature as a part of the vessel map, is using combination of RT, overlapping windows, and morphological reconstruction to distinguish between MAs and segmented vessels by selecting an appropriate window size, n, and an accurate reconstruction process. Moreover, as we have already mentioned in Section 3.3.1, the window size is also important in our final results to identify bifurcation point, and branching point vessel pixels. If the window is too large, we may be unable to estimate the curvature of blood vessel and also unable to detect the thin blood vessels in the presence of noise. The retinal blood vessel's curvature can be estimated with lines as long as an appropriate window size is applied. If the window size is too small, we are unable to generate clear Radon peaks in the Radon space in the presence of noise. Branching points also face with difficulty if the size of window is too small. We have applied structural similarity approach as an alternative motivating principle as a criterion for quality of our automated vessel segmentation based on the SSIM index. From an image segmentation point of view, we considered this SSIM indexing method as a particular implementation of the philosophy of structural similarity. We compared our evaluation using SSIM with some important works [47, 56, 59, 61, 62, 94] (see Table 9). The results show that our proposed method is as good as other or even better than some of them.

From deep learning view point, we have some excellent studies, which we mentioned them in Section 2, with very good results [68–75, 77, 99]. As a whole, our results are close to most of these studies [73–75] or less than some of them like [68, 77]. However, the problem of these methods is that they need huge database for learning purpose, and if we have that, using these methods will be very useful. As an interesting extension of this work to be pursued in future studies is combining concept of deep NN with current study and improve the results.

However, our approach has one limitation. From computational viewpoint, some approaches such as [46, 59–62] are much faster and this is a main drawback of the proposed approach. The average processing time for these studies are less than a minute. For some of them, like [46, 61], it is less than 10 s. However, the average processing time for our method running on a PC with an Intel Corei3 CPU at 2.13 GHz and 2

GB of RAM was 2.5 min, which is likely to be too high for portable DR screening systems of the future. The reason for this arises from the use of the RT in overlapping windows. Without overlapping windows, the computational time is less than a minute, which is acceptable, but in this case, as we have shown in Table 4, the accuracy of vessel segmentation tremendously will drop. Another future work will be directed toward computational analysis of the MUMS-DB database, because it is large, even though biased towards images with disease, with some fast approaches with high accuracy such as [46, 59–61] to test the performance of our algorithm with them from both a computational and the accuracy view point. However, the timings for our algorithm are quoted for an implementation in Matlab, and are certainly be transformable to speed-up in other languages, such as CSharp. Moreover, as we point out before, the focus of this study is on high accuracy of diagnosis DR and robustness of the algorithm.

7 | CONCLUSION

An important feature of the study is the use of the RT to detect the vascular tree in fundus images, and the use of morphological reconstruction operators. Computers are appropriate for problems involving the derivation of quantitative information from images because their capacity to process data is fast and effective and has a high level of reproducibility [100]. Moreover, an automatic system would help to reduce the workload of well-paid ophthalmologists, enabling hospitals and eye clinics to use their resources in other important tasks [101]. In addition, the detection of the retinal blood vessel tree can facilitate detection of other features that are signs of disease, such as MAs, HEs, and other changes in the vascular network including neovascularization and venous changes.

The quality of our segmentation depends on some parameters such as the size of the window, window step, and line validation thresholding. Determining appropriate values for these parameters has some advantages in the processing including: accurate detection of retinal vessels location, determination of some parameters like width and length of vessels, and even determining the location of vessel bifurcation, which can assist clinicians in analysing images later by registration schemes.

Our algorithm also has some important characteristics in the detection of vascular structure in retinal images that include its robustness to noise, because of the characteristic of the algorithm which is an integral transformation; acceptable performance in the detection of both thick and thin vessels by the combined methods of RT and multi-overlapping windows; and last but not least, the method is simple in comparison with other methods mentioned in this paper.

ACKNOWLEDGMENTS

The authors would like to thank J.J. Staal and his colleagues, A. Hoover, and Fraz and his colleagues for making their databases publicly available.

REFERENCES

1. Abràmoff, M.D., et al.: Evaluation of a system for automatic detection of diabetic retinopathy from color fundus photographs in a large population of patients with diabetes. Diabetes Care 31, 193–198 (2008)
2. Sasongko, M., et al.: Retinal vascular tortuosity in persons with diabetes and diabetic retinopathy. Diabetologia 54, 2409–2416 (2011)
3. Zhou, W., et al.: Automatic microaneurysm detection using the sparse principal component analysis-based unsupervised classification method. IEEE Access 5, 2563–2572 (2017)
4. Abràmoff, M.D., Garvin, M.K., Sonka, M.: Retinal imaging and image analysis. IEEE Rev. Biomed. Eng. 3, 169–208 (2010)
5. Palomera-Pérez, M.A., et al.: Parallel multiscale feature extraction and region growing: Application in retinal blood vessel detection. IEEE Trans. Inf. Technol. Biomed. 14, 500–506 (2009)
6. Tavakoli, M., et al.: A complementary method for automated detection of microaneurysms in fluorescein angiography fundus images to assess diabetic retinopathy. Pattern Recognit. 46, 2740–2753 (2013)
7. Mookiah, M.R.K., et al.: Computer-aided diagnosis of diabetic retinopathy: A review. Comput. Biol. Med. 43, 2136–2155 (2013)
8. Faust, O., et al.: Algorithms for the automated detection of diabetic retinopathy using digital fundus images: a review. J. Med. Syst. 36, 145–157 (2012)
9. Mendonca, A.M., Campilho, A.: Segmentation of retinal blood vessels by combining the detection of centerlines and morphological reconstruction. IEEE Trans. Med. Imaging 25, 1200–1213 (2006)
10. Welikala, R., et al.: Automated detection of proliferative diabetic retinopathy using a modified line operator and dual classification. Comput. Methods Programs Biomed. 114, 247–261 (2014)
11. Welikala, R., et al.: Genetic algorithm based feature selection combined with dual classification for the automated detection of proliferative diabetic retinopathy. Comput. Med. Imaging Graph. 43, 64–77 (2015)
12. Chaudhuri, S., et al.: Detection of blood vessels in retinal images using two-dimensional matched filters. IEEE Trans. Med. Imaging 8, 263–269 (1989)
13. Youssif, A.A.-H.A.-R., Ghalwash, A.Z., Ghoneim, A.A.S.A.-R.: Optic disc detection from normalized digital fundus images by means of a vessels' direction matched filter. IEEE Trans. Med. Imaging 27, 11–18 (2008)
14. Aquino, A., Gegúndez-Arias, M.E., Marín, D.: Detecting the optic disc boundary in digital fundus images using morphological, edge detection, and feature extraction techniques. IEEE Trans. Med. Imaging 29, 1860–1869 (2010)
15. Tavakoli, M., et al.: Automated fovea detection based on unsupervised retinal vessel segmentation method. In: 2017 IEEE Nuclear Science Symposium and Medical Imaging Conference (NSS/MIC). IEEE, pp. 1–7 (2017)
16. Tavakoli, M., et al.: Radon transform technique for linear structures detection: Application to vessel detection in fluorescein angiography fundus images. In: Nuclear Science Symposium and Medical Imaging Conference (NSS/MIC). IEEE, pp. 3051–3056 (2011)
17. Wang, Z., et al.: Image quality assessment: From error visibility to structural similarity. IEEE Trans. Image Process. 13, 600–612 (2004)
18. Deans, S.R.: The Radon Transform and Some of Its Applications. Dover Publications, INC., NewYork (2007)
19. Zhang, Q., Couloigner, I.: Accurate centerline detection and line width estimation of thick lines using the radon transform. IEEE Trans. Image Process. 16, 310–316 (2007)
20. Odstrcilik, J., et al.: Retinal vessel segmentation by improved matched filtering: Evaluation on a new high-resolution fundus image database. IET Image Proc. 7, 373–383 (2013)
21. Franklin, S.W., Rajan, S.E.: Computerized screening of diabetic retinopathy employing blood vessel segmentation in retinal images. Biocybern. Biomed. Eng. 34, 117–124 (2014)
22. Estrada, R., et al.: Retinal artery-vein classification via topology estimation. IEEE Trans. Med. Imaging 34, 2518–2534 (2015)
23. Zhang, L., Fisher, M., Wang, W.: Retinal vessel segmentation using multiscale textons derived from keypoints. Comput. Med. Imaging Graph. 45, 47–56 (2015)

24. Dashtbozorg, B., Mendonça, A.M., Campilho, A.: An automatic graph-based approach for artery/vein classification in retinal images. IEEE Trans. Image Process. 23, 1073–1083 (2014)
25. Zhao, Y.Q., et al.: Retinal vessels segmentation based on level set and region growing. Pattern Recognit. 47, 2437–2446 (2014)
26. Kovács, G., Hajdu, A.: A self-calibrating approach for the segmentation of retinal vessels by template matching and contour reconstruction. Med. Image Anal. 29, 24–46 (2016)
27. Lázár, I., Hajdu, A.: Segmentation of retinal vessels by means of directional response vector similarity and region growing. Comput. Biol. Med. 66, 209–221 (2015)
28. Fraz, M.M., et al.: An ensemble classification-based approach applied to retinal blood vessel segmentation. IEEE Trans. Biomed. Eng. 59, 2538–2548 (2012)
29. Fraz, M.M., et al.: An approach to localize the retinal blood vessels using bit planes and centerline detection. Comput. Methods Programs Biomed. 108, 600–616 (2012)
30. Panda, R., Puhan, N., Panda, G.: New binary Hausdorff symmetry measure based seeded region growing for retinal vessel segmentation. Biocybern. Biomed. Eng. 36, 119–129 (2016)
31. Xu, X., et al.: Vessel boundary delineation on fundus images using graph-based approach. IEEE Trans. Med. Imaging 30, 1184–1191 (2011)
32. Akram, M.U., Khan, S.A.: Multilayered thresholding-based blood vessel segmentation for screening of diabetic retinopathy. Eng. Comput. 29, 165–173 (2013)
33. Orlando, J.I., Prokofyeva, E., Blaschko, M.B.: A discriminatively trained fully connected conditional random field model for blood vessel segmentation in fundus images. IEEE Trans. Biomed. Eng. 64, 16–27 (2017)
34. Neto, L.C., et al.: An unsupervised coarse-to-fine algorithm for blood vessel segmentation in fundus images. Expert Syst. Appl. 78, 182–192 (2017)
35. Jiang, Z., et al.: Fast, accurate and robust retinal vessel segmentation system. Biocybern. Biomed. Eng. 37, 412–421 (2017)
36. Farokhian, F., et al.: Automatic parameters selection of Gabor filters with the imperialism competitive algorithm with application to retinal vessel segmentation. Biocybern. Biomed. Eng. 37, 246–254 (2017)
37. Biswal, B., Pooja, T., Subrahmanyam, N.B.: Robust retinal blood vessel segmentation using line detectors with multiple masks. IET Image Proc. 12, 389–399 (2017)
38. Karn, P.K., Biswal, B., Samantaray, S.R.: Robust retinal blood vessel segmentation using hybrid active contour model. IET Image Proc. 13, 440–450 (2018)
39. Yue, K., et al.: Improved multi-scale line detection method for retinal blood vessel segmentation. IET Image Proc. 12, 1450–1457 (2018)
40. Sathananthavathi, V., Indumathi, G.: Bat algorithm inspired retinal blood vessel segmentation. IET Image Proc. 12, 2075–2083 (2018)
41. Khomri, B., et al.: Retinal blood vessel segmentation using the elite-guided multi-objective artificial bee colony algorithm. IET Image Proc. 12, 2163–2171 (2018)
42. Wang, W., Wang, W., Hu, Z.: Retinal vessel segmentation approach based on corrected morphological transformation and fractal dimension. IET Image Proc. 13, 2538–2547 (2019)
43. Fraz, M.M., et al.: Blood vessel segmentation methodologies in retinal images-A survey. Comput. Methods Programs Biomed. 108, 407–433 (2012)
44. Moccia, S., et al.: Blood vessel segmentation algorithms–review of methods, datasets and evaluation metrics. Comput. Methods Programs Biomed. 158, 71–91 (2018)
45. Annunziata, R., et al.: Leveraging multiscale hessian-based enhancement with a novel exudate inpainting technique for retinal vessel segmentation. IEEE J. Biomed. Health. Inf. 20, 1129–1138 (2016)
46. Roychowdhury, S., Koozekanani, D.D., Parhi, K.K.: Blood vessel segmentation of fundus images by major vessel extraction and subimage classification. IEEE J. Biomed. Health. Inf. 19, 1118–1128 (2015)
47. Hoover, A., Kouznetsova, V., Goldbaum, M.: Locating blood vessels in retinal images by piecewise threshold probing of a matched filter response. IEEE Trans. Med. Imaging 19, 203–210 (2000)
48. Chakraborti, T., et al.: A self-adaptive matched filter for retinal blood vessel detection. Mach. Vision Appl. 26, 55–68 (2015)
49. Imani, E., Javidi, M., Pourreza, H.-R.: Improvement of retinal blood vessel detection using morphological component analysis. Comput. Methods Programs Biomed. 118, 263–279 (2015)
50. Martinez-Perez, M.E., et al.: Segmentation of blood vessels from red-free and fluorescein retinal images. Med. Image Anal. 11, 47–61 (2007)
51. Zhang, J., et al.: Robust retinal vessel segmentation via locally adaptive derivative frames in orientation scores. IEEE Trans. Med. Imaging 35, 2631–2644 (2016)
52. Nguyen, U.T., et al.: An effective retinal blood vessel segmentation method using multi-scale line detection. Pattern Recognit. 46, 703–715 (2013)
53. Vermeer, K.A., et al.: A model based method for retinal blood vessel detection. Comput. Biol. Med. 34, 209–219 (2004)
54. Lam, B.S.Y., Yan, H.: A novel vessel segmentation algorithm for pathological retina images based on the divergence of vector fields. IEEE Trans. Med. Imaging 27, 237–246 (2008)
55. Niemeijer, M., et al.: Comparative study of retinal vessel segmentation methods on a new publicly available database. In: SPIE Medical Imaging Conference. SPIE, vol. 5370, pp. 648–656. (2004)
56. Soares, J.V., et al.: Retinal vessel segmentation using the 2-D Gabor wavelet and supervised classification. IEEE Trans. Med. Imaging 25, 1214–1222 (2006)
57. Ricci, E., Perfetti, R.: Retinal blood vessel segmentation using line operators and support vector classification. IEEE Trans. Med. Imaging 26, 1357–1365 (2007)
58. Lupascu, C.A., Tegolo, D., Trucco, E.: FABC: retinal vessel segmentation using AdaBoost. IEEE Trans. Inf. Technol. Biomed. 14, 1267–1274 (2010)
59. Marín, D., et al.: A new supervised method for blood vessel segmentation in retinal images by using gray-level and moment invariants-based features. IEEE Trans. Med. Imaging 30, 146–158 (2011)
60. Jiang, X., Mojon, D.: Adaptive local thresholding by verification-based multithreshold probing with application to vessel detection in retinal images. IEEE Trans. Pattern Anal. Mach. Intell. 25, 131–137 (2003)
61. Roychowdhury, S., Koozekanani, D.D., Parhi, K.K.: Iterative vessel segmentation of fundus images. IEEE Trans. Biomed. Eng. 62, 1738–1749 (2015)
62. Azzopardi, G., et al.: Trainable cosfire filters for vessel delineation with application to retinal images. Med. Image Anal. 19, 46–57 (2015)
63. Wu, D., et al.: On the adaptive detection of blood vessels in retinal images. IEEE Trans. Biomed. Eng. 53, 341–343 (2006)
64. Tolias, Y.A., Panas, S.M.: A fuzzy vessel tracking algorithm for retinal images based on fuzzy clustering. IEEE Trans. Med. Imaging 17, 263–273 (1998)
65. Thangaraj, S., Periyasamy, V., Balaji, R.: Retinal vessel segmentation using neural network. IET Image Proc. 12, 669–678 (2017)
66. Staal, J., et al.: Ridge-based vessel segmentation in color images of the retina. IEEE Trans. Med. Imaging 23, 501–509 (2004)
67. Sinthanayothin, C., et al.: Automated localisation of the optic disc, fovea, and retinal blood vessels from digital colour fundus images. Brit. J. Ophthalmol. 83, 902–910 (1999)
68. Li, Q., et al.: A cross-modality learning approach for vessel segmentation in retinal images. IEEE Trans. Med. Imaging 35, 109–118 (2016)
69. Annunziata, R., Trucco, E.: Accelerating convolutional sparse coding for curvilinear structures segmentation by refining SCIRD-TS filter banks. IEEE Trans. Med. Imaging 35, 2381–2392 (2016)
70. Wang, S., et al.: Hierarchical retinal blood vessel segmentation based on feature and ensemble learning. Neurocomputing 149, 708–717 (2015)
71. Zhu, C., et al.: Retinal vessel segmentation in colour fundus images using extreme learning machine. Comput. Med. Imaging Graph. 55, 68–77 (2017)
72. Tan, J.H., et al.: Segmentation of optic disc, fovea and retinal vasculature using a single convolutional neural network. J. Comput. Sci. 20, 70–79 (2017)
73. Liskowski, P., Krawiec, K.: Segmenting retinal blood vessels with deep neural networks. IEEE Trans. Med. Imaging 35, 2369–2380 (2016)

74. Lin, Y., Zhang, H., Hu, G.: Automatic retinal vessel segmentation via deeply supervised and smoothly regularized network. IEEE Access 7, 57717–57724 (2018)
75. Ren, X., et al.: Drusen segmentation from retinal images via supervised feature learning. IEEE Access 6, 2952–2961 (2018)
76. Oliveira, A., Pereira, S., Silva, C.A.: Retinal vessel segmentation based on fully convolutional neural networks. Expert Syst. Appl. 112, 229–242 (2018)
77. Rammy, S.A., et al.: CPGAN: Conditional patch-based generative adversarial network for retinal vessel segmentation. IET Image Proc. 14, 1081–1090 (2019)
78. Pourreza-Shahri, R., Tavakoli, M., Kehtarnavaz, N.: Computationally efficient optic nerve head detection in retinal fundus images. Biomed. Signal Process. Control 11, 63–73 (2014)
79. Soille, P.: Morphological Image Analysis: Principles and Applications. springer-Verlag, New York (2013)
80. Wang, Z., Bovik, A.C., Lu, L.: Why is image quality assessment so difficult? In: IEEE International Conference on Acoustics, Speech, and Signal Processing (ICASSP). IEEE, vol. 4, pp. IV–3313 (2002)
81. Brooks, A.C., Zhao, X., Pappas, T.N.: Structural similarity quality metrics in a coding context: Exploring the space of realistic distortions. IEEE Trans. Image Process. 17, 1261–1273 (2008)
82. Saito, T., Rehmsmeier, M.: The precision-recall plot is more informative than the ROC plot when evaluating binary classifiers on imbalanced datasets. PloS One 10, e0118432 (2015)
83. Tavakoli, M., et al.: Automated optic nerve head detection in fluorescein angiography fundus images. In: Nuclear Science Symposium and Medical Imaging Conference (NSS/MIC), IEEE, pp. 3057–3060 (2011)
84. Yan, Z., Yang, X., Cheng, K.-T.: A skeletal similarity metric for quality evaluation of retinal vessel segmentation. IEEE Trans. Med. Imaging 37, 1045–1057 (2018)
85. Cheng, E., et al.: Discriminative vessel segmentation in retinal images by fusing context-aware hybrid features. Mach. Vision Appl. 25, 1779–1792 (2014)
86. Fawcett, T.: An introduction to ROC analysis. Pattern Recognit. Lett. 27, 861–874 (2006)
87. Zhao, Y., et al.: Automated vessel segmentation using infinite perimeter active contour model with hybrid region information with application to retinal images. IEEE Trans. Med. Imaging 34, 1797–1807 (2015)
88. Ayerdi, B., Graña, M.: Random forest active learning for retinal image segmentation. In: Proceedings of the 9th International Conference on Computer Recognition Systems (CORES) 2015. Springer, Switzerland pp. 213–221 (2016)
89. Oliveira, W.S., et al.: Unsupervised retinal vessel segmentation using combined filters. PloS One 11, e0149943 (2016)
90. Zhao, Y., et al.: Correction: Retinal vessel segmentation: An efficient graph cut approach with retinex and local phase. PloS One 10, e0127486 (2015)
91. Javidi, M., Pourreza, H.-R., Harati, A.: Vessel segmentation and microaneurysm detection using discriminative dictionary learning and sparse representation. Comput. Methods Programs Biomed. 139, 93–108 (2017)
92. Shahid, M., Taj, I.A.: Robust retinal vessel segmentation using vessel's location map and Frangi enhancement filter. IET Image Proc. 12, 494–501 (2018)
93. Cinsdikici, M.G., Aydın, D.: Detection of blood vessels in ophthalmoscope images using MF/ANT (matched filter/ant colony) algorithm. Comput. Methods Programs Biomed. 96, 85–95 (2009)
94. Lam, B.S., Gao, Y., Liew, A.W.-C.: General retinal vessel segmentation using regularization-based multiconcavity modeling. IEEE Trans. Med. Imaging 29, 1369–1381 (2010)
95. Zana, F., Klein, J.-C.: A multimodal registration algorithm of eye fundus images using vessels detection and hough transform. IEEE Trans. Med. Imaging 18, 419–428 (1999)
96. Gang, L., Chutatape, O., Krishnan, S.M.: Detection and measurement of retinal vessels in fundus images using amplitude modified second-order gaussian filter. IEEE Trans. Biomed. Eng. 49, 168–172 (2002)
97. Gelman, R., et al.: Diagnosis of plus disease in retinopathy of prematurity using retinal image multiscale analysis. Invest. Ophthalmol. Visual Sci. 46, 4734–4738 (2005)
98. Martinez-Perez, M.E., et al.: Retinal vascular tree morphology: A semi-automatic quantification. IEEE Trans. Biomed. Eng. 49, 912–917 (2002)
99. Fu, H., et al.: Retinal vessel segmentation via deep learning network and fully-connected conditional random fields. In: IEEE 13th International Symposium on Biomedical Imaging (ISBI). IEEE, pp. 698–701 (2016)
100. Seoud, L., et al.: Red lesion detection using dynamic shape features for diabetic retinopathy screening. IEEE Trans. Med. Imaging 35, 1116–1126 (2016)
101. Tavakoli, M., Nazar, M., Mehdizadeh, A.: Effect of two different preprocessing steps in detection of optic nerve head in fundus images. In: SPIE Medical Imaging. International Society for Optics and Photonics, SPIE, Orlando, USA pp. 101343A–101343A (2017)

How to cite this article: Tavakoli M, Mehdizadeh A, Shahri RP, Dehmeshki J. Unsupervised automated retinal vessel segmentation based on Radon line detector and morphological reconstruction. *IET Image Process.* 2021;15:1484–1498.
https://doi.org/10.1049/ipr2.12119